RESEARCH ARTICLE

Key Points:
- Empirical orthogonal function analysis in both spatial and spectral domains
- Optimal space grid for empirical orthogonal function analysis
- Analysis of two uncorrelated jerk patterns in the CM4 model

Correspondence to:
M. A. Pais,
pais@fis.uc.pt

Time-correlated patterns from spherical harmonic expansions: Application to geomagnetism

M. A. Pais[1,2], P. Alberto[3], and F. J. G. Pinheiro[1]

[1]CITEUC, Geophysical and Astronomical Observatory, University of Coimbra, Coimbra, Portugal, [2]Department of Physics, University of Coimbra, Coimbra, Portugal, [3]CFisUC, Department of Physics, University of Coimbra, Coimbra, Portugal

Abstract We use empirical orthogonal function analysis (EOFA) directly on sets of Schmidt spherical harmonic (SH) coefficients modeling the internal geomagnetic field or its time derivatives at different epochs. We show how to properly use the method such that the application of EOFA to either spatial or spectral domains leads to the same results, bypassing the need to work on snapshots of field charts synthesized from SHs. In case a spatial grid is required, we point out which is the best grid to use. We apply the method to the CM4 geomagnetic field model to illustrate the differences in EOFA modes obtained with and without corrections. Once the corrected main modes of secular acceleration (SA) have been singled out, we retrieve previous results showing that the 1969, 1978, and 1991 geomagnetic field acceleration jumps have the same spatial pattern. A new finding in this study is that the same spatial pattern is present in principal modes of secular variation which, once inverted, may provide the flow responsible for the jerk sequence. Another finding is the unveiling of a different spatial structure common to a second group of jerks with SA pulses around 1985 and 1996, displaying a localization very similar to SA pulses identified in 2006 and 2009 using recent satellite data. Finally, if properly handled, the EOFA can be directly applied to a grid of data values of the geomagnetic field in order to produce SH models of decorrelated modes which may help to separate different sources of the field.

1. Introduction

Empirical orthogonal function analysis (EOFA) (often called principal component analysis) is a multivariate data analysis technique used to extract spatial coherent structures that evolve correlated in time. The method has been extensively used in meteorology and oceanography, on data consisting of time-evolving grids of a certain geophysical field as pressure, temperature, or zonal winds [e.g., *Preisendorfer*, 1988; *Peixoto and Oort*, 1992].

A large number of applications can be found in the fields of geomagnetism and aeronomy. Since the 1970s, the method has been applied under the name of natural orthogonal component (NOC) decomposition, to separate quiet and disturbed magnetic field variations or longer and shorter wavelength components [*Faynberg*, 1975; *Pushkov et al.*, 1976; *Golovkov et al.*, 1978]. An account of the NOC formalism used in those studies is given by *Langel* [1987]. In empirical ionospheric modeling, *Daniell et al.* [1995] applied EOFA to decompose the altitude profiles of ion concentration in terms of orthogonal functions obtained during the calculation procedure and revealing the coherent structures of the original data. *Xu and Kamide* [2004] applied the method to the analysis of geomagnetic daily variation observed at Beijing Ming Tombs observatory all over the year 2001, trying to understand the observed day-to-day variability. In studies of global-scale electromagnetic induction in the Earth's mantle by long-period geomagnetic field variations, EOFA has been applied to data in the time domain as well as in the Fourier transform domain, to estimate spatially and temporally coherent external source (inducing) current systems [*Fujii and Schultz*, 2002; *Balasis and Egbert*, 2006].

Studies more focused on the core field applied the NOC method with the goal to remove components from external sources in internal geomagnetic field modeling [*Pushkov et al.*, 1976; *Golovkov et al.*, 1978, 2005] or to single out certain periodicities of the main field [*Rotanova et al.*, 1982]. Also referring to NOC, *Xu* [2002, 2003] analyzed the variability of Gauss coefficients g_ℓ^m and h_ℓ^m of the main field from 21 International Geomagnetic Reference Field models for 1900–2000 at 5 year interval, the main goal being to revise the spherical harmonic (SH) model in periods of higher uncertainty. More recently, *Chulliat and Maus* [2014] applied the method to SH Hann-filtered coefficients of geomagnetic field secular acceleration models ($\ddot{g}_\ell^m$ and $\ddot{h}_\ell^m$), calculated from

3 year time intervals of CHAMP data from January 2001 to September 2010. They identified a certain spatial pattern, recurrently activated at the time of recent 2003, 2007, and 2011 jerks. Working on flows inverted from geomagnetic field models, *Pais et al.* [2015] applied the method to a regular spatial grid of values of the pseudo-stream function for the quasi-geostrophic flow outside the tangent cylinder.

In all those studies EOFA has been used with three main different goals. In some cases, the objective was to separate contributions from different sources to the scalar field under scrutiny, for a better understanding of those sources [*Golovkov et al.*, 2005; *Fujii and Schultz*, 2002; *Balasis and Egbert*, 2006; *Pais et al.*, 2015]. This was based on the assumption that the fields caused by different processes in different media are expected to have different spatial patterns that do not correlate in time. In other studies, the main purpose was to build an empirical model of the data excluding nonrelevant information [*Daniell et al.*, 1995], by considering the contribution of only a few main modes. Finally, there are also applications of the method that aspire to correct noisy data [e.g., *Xu*, 2002], by eliminating uncorrelated modes.

In some examples, the time-space data matrix to which EOFA is applied is built directly from observations or synthesized from an existing model consisting in a set of time-dependent SH coefficients. It is the case of most applications in meteorology and oceanography and the inverted core flows application in *Pais et al.* [2015]. In other cases, the method is applied to a "data" matrix of time-varying SH coefficients [*Golovkov et al.*, 1978, 2005; *Xu*, 2002, 2003; *Chulliat and Maus*, 2014]. A large number of references explain how to use the EOF method with a time-space data matrix, and another set of references shows how to use it with a time-SH coefficients matrix. We have not found, however, any explicit account of how to assure that the EOFA results retrieved on the spherical harmonic domain can be correctly transformed to the space domain, and vice versa. In this paper we show that applying directly EOFA to spherical harmonic models must be done in a particular way, if results are to be independent of both the normalization used for spherical harmonic functions and the domain (spatial or spectral) where EOFA is applied. A unique definition for each mode is required, if some physical interpretation is envisaged for the computed principal components and empirical orthogonal functions. This discussion acquires special relevance in the field of geomagnetism, as we will show, because of the standard usage of Schmidt normalization for SH coefficients and harmonic functions, instead of a full normalization. Applications found using Gravity Recovery and Climate Experiment gravity data [e.g., *Wouters and Schrama*, 2007], where fully normalized Stokes coefficients and associated Legendre functions are used, do not suffer as strongly from this ambiguity.

Once the correct application of EOFA on SH models will be made clear, the relevance of this study for the understanding of some specific features of the geomagnetic field variability will be shown. The proposed corrections are illustrated using the internal component of the CM4 model [*Sabaka et al.*, 2004]. This component is known to reproduce the observed jerks of 1969, 1978, and 1991 in a number of observatories. In particular, the similarity of spatial patterns associated to the jump in the geomagnetic acceleration field at those epochs and first noticed by *Le Huy et al.* [1998] is reproduced by the model, as well as the anticorrelation of successive events.

In section 2 we introduce the notation and expose the problem we will be dealing with: how do EOFA components obtained from spatial data grids and from sets of SH coefficients relate to each other? In section 3 we derive the algebraic relations that show how time-space matrices and time-SH coefficient matrices should be transformed before the EOF method is applied, in order to find the same modes in space and spectral domains. An error is unavoidable when going from the description of the modes in terms of SH coefficients to the modes in a spatial grid. This error is nonetheless brought to negligible levels when using a spatial grid built from Gauss-Legendre quadrature points as shown in Appendix B. An estimation of errors will be done as a function of the kind of grid and the grid resolution. In section 4 we apply the method to the geomagnetic field model CM4. In section 5 we show how the results in this paper can contribute to bring new insight into relevant questions under debate.

2. EOFA Applied to Spatial Grid Values and to SH Coefficients

We summarize the EOFA formalism, which is standard and has a large number of bibliographic support [e.g., *Preisendorfer*, 1988], following closely *Pais et al.* [2015]. For an easier reading of sections 2 and 3 a list of symbols used in these two sections, with their corresponding meanings, is provided in Table 1.

Table 1. List of Symbols in Sections 2 and 3

Symbol	Definition
$\mathbf{X}$	Data matrix $n_{\text{epoch}} \times n_{\text{point}}$, with X_{ij} the scalar field X at time t_i and at point $\vec{r}_j$.
$\mathbf{C}_X$	Covariance matrix of $\mathbf{X}$: $\mathbf{C}_X = \mathbf{X}^T\mathbf{X}$.
$\mathbf{S}$	Data matrix $n_{\text{epoch}} \times n_{\text{coef}}$, with S_{ij} the Schmidt normalized SH coefficient $j = \{\ell, m\}$ of degree ℓ and order m, at time t_i.
$\mathbf{C}_S$	Covariance matrix of $\mathbf{S}$: $\mathbf{C}_S = \mathbf{S}^T\mathbf{S}$.
$\mathbf{F}$	Transformation matrix $n_{\text{point}} \times n_{\text{coef}}$ from a spectral to a spatial description of X: $\mathbf{X} = \mathbf{SF}^T$.
$\mathbf{G}$	Diagonal matrix $n_{\text{point}} \times n_{\text{point}}$ with elements $G_{ii} = \sqrt{\Delta\theta\Delta\phi\sin\theta_i}$.
$\mathbf{N}$	Diagonal matrix $n_{\text{coef}} \times n_{\text{coef}}$ with elements $N_{ii} = \sqrt{4\pi/(2\ell_i + 1)}$.
$\mathbf{X}'$	Data matrix corrected for overrepresentation of higher latitudes: $\mathbf{X}' = \mathbf{XG}^T$.
$\mathbf{C}_{X'}$	Covariance matrix of $\mathbf{X}'$: $\mathbf{C}_{X'} = \mathbf{X}'^T\mathbf{X}'$.
$\mathbf{S}'$	Data matrix $\mathbf{S}$ corrected for Schmidt normalization: $\mathbf{S}' = \mathbf{SN}^T$.
$\mathbf{C}_{S'}$	Covariance matrix of $\mathbf{S}'$: $\mathbf{C}_{S'} = \mathbf{S}'^T\mathbf{S}'$.
$\mathbf{F}'$	Transformation matrix: $\mathbf{X}' = \mathbf{S}'\mathbf{F}'^T$.
$\mathbf{P}$	Orthogonal matrix $n_{\text{point}} \times n_{\text{point}}$ with EOFs of $\mathbf{X}$ as columns.
$\mathbf{Y}$	Matrix $n_{\text{epoch}} \times n_{\text{point}}$ with temporal variation of the EOFs of $\mathbf{X}$ as columns: $\mathbf{X} = \mathbf{YP}^T$.
$\lambda_{X,i}$	Singular values of $\mathbf{X}$.
$\mathbf{\Lambda}_X$	Diagonal matrix $n_{\text{point}} \times n_{\text{point}}$ with elements $\Lambda_{X,ii} = \lambda_{X,i}^2$ ordered by decreasing value.
$\mathbf{Q}$	Orthogonal matrix $n_{\text{coef}} \times n_{\text{coef}}$ with EOFs of $\mathbf{S}$ as columns.
$\mathbf{Z}$	Matrix $n_{\text{epoch}} \times n_{\text{coef}}$ with temporal variation of the EOFs of $\mathbf{S}$ as columns: $\mathbf{S} = \mathbf{ZQ}^T$.
$\lambda_{S,i}$	Singular values of $\mathbf{S}$.
$\mathbf{\Lambda}_S$	Diagonal matrix $n_{\text{coef}} \times n_{\text{coef}}$ with elements $\Lambda_{S,ii} = \lambda_{S,i}^2$ ordered by decreasing value.
$\mathbf{P}'$	Orthogonal matrix with EOFs of $\mathbf{X}'$ as columns.
$\mathbf{Y}'$	Matrix with temporal variation of the EOFs of $\mathbf{X}'$ as columns: $\mathbf{X}' = \mathbf{Y}'\mathbf{P}'^T$.
$\lambda_{X',i}$	Singular values of $\mathbf{X}'$.
$\mathbf{\Lambda}_{X'}$	Diagonal matrix with elements $\Lambda_{X',ii} = \lambda_{X',i}^2$ ordered by decreasing value.
$\mathbf{Q}'$	Orthogonal matrix with EOFs of $\mathbf{S}'$ as columns.
$\mathbf{Z}'$	Matrix with temporal variation of the EOFs of $\mathbf{S}'$ as columns: $\mathbf{S}' = \mathbf{Z}'\mathbf{Q}'^T$.
$\lambda_{S',i}$	Singular values of $\mathbf{S}'$.
$\mathbf{\Lambda}_{S'}$	Diagonal matrix with elements $\Lambda_{S',ii} = \lambda_{S',i}^2$ ordered by decreasing value.

When applying EOFA to a time-dependent scalar field sampled on a regular spatial grid, $\mathbf{X}$ will stand for the data matrix. Each element $X_{ij} \equiv X(t_i, \vec{r}_j)$ is the value of the field at point $\vec{r}_j$ at time t_i, once the time average during the analyzed period has been subtracted. The index i takes values from 1 to the total number of epochs, n_{epoch}, and the index j takes values from 1 to the total number of points in the grid, n_{point}. The EOF analysis relies on the description of the space-time data in terms of decorrelated modes. They are the eigenvectors of the covariance matrix $\mathbf{C}_X = \mathbf{X}^T\mathbf{X}$. We denote $\mathbf{P}$ as the orthogonal matrix of eigenvectors of $\mathbf{C}_X$, with columns containing the separate coherent spatial structures called empirical orthogonal functions (EOFs), normalized and described in terms of the chosen grid. Projecting the data matrix onto $\mathbf{P}$ recovers the time evolution of each EOF, as given by columns of matrix $\mathbf{Y}$ such that $\mathbf{Y} = \mathbf{XP}$. The time series in columns of $\mathbf{Y}$ are the normalized principal components (PCs) multiplied by $\lambda_{X,i}$, the square roots of the $\mathbf{C}_X$ eigenvalues (or singular values of $\mathbf{X}$). The different EOFs in columns of $\mathbf{P}$ and the different PCs in columns of $\mathbf{Y}$ are arranged in order of decreasing values of $\lambda_{X,i}$. The set of $\lambda_{X,i}$ gives information on the relevance of the corresponding EOFA modes to explain the data variability, the percentage of data variance explained by mode i being computed as

$$f_i = \lambda_{X,i}^2 / \left(\sum_k \lambda_{X,k}^2 \right) . \tag{1}$$

The $\lambda_{X,i}$ values are all positive or zero. Different $\lambda_{X,i}$ values squared can be found as elements of the diagonal matrix $\mathbf{\Lambda}_X = \mathbf{Y}^T\mathbf{Y}$, ordered from the larger to the smaller.

The original data can be expressed in terms of the decorrelated modes as

$$\mathbf{X} = \mathbf{Y}\mathbf{P}^T \tag{2}$$

or, equivalently,

$$\mathbf{X} = \sum_i \lambda_{X,i} (\mathbf{PC})_i (\mathbf{EOF})_i^T \tag{3}$$

where $\lambda_{X,i}$ $(\mathbf{PC})_i$, and $(\mathbf{EOF})_i$ are columns i of matrices $\mathbf{Y}$ and $\mathbf{P}$, respectively, containing the time and space structures of EOFA mode i. Note that (3) may be described as the singular value decomposition of matrix $\mathbf{X}$. In practice, only the first few modes are important (first columns of $\mathbf{Y}$ and lines of $\mathbf{P}^T$), those that explain the highest percentage of data variance as given by (1).

Let us now suppose that the scalar field sampled at the regular grid is obtained from a SH model. From global Earth coverages of a certain geophysical field (e.g., the gravity or the geomagnetic fields) during a certain time interval, a set of spherical harmonic coefficients $s_\ell^m(t)$ can be computed. These coefficients must retrieve the observed field at a certain point $\vec{r}_j$ (and within a certain model precision):

$$X(t_i, \vec{r}_j) = \sum_{\ell,m}^{\ell_{max}} s_\ell^m(t_i) f_\ell^m(\theta_j, \phi_j) . \tag{4}$$

Using the index k for each combination of $\{\ell, m\}$ coefficients, we can write

$$X(t_i, \vec{r}_j) = \sum_k^{n_{coef}} s(t_i, k) f(\theta_j, \phi_j, k) , \tag{5}$$

which in matrix form yields

$$\mathbf{X} = \mathbf{S}\mathbf{F}^T . \tag{6}$$

Matrix $\mathbf{F}$ of elements $F_{jk} = f(\theta_j, \phi_j, k)$ is the transformation matrix from a spectral to a spatial grid description of the field, having in column $k = \{\ell, m\}$ the spherical harmonic function f_ℓ^m discretized at all $j = 1, \cdots, n_{point}$ grid points. $\mathbf{F}$ does not depend on time, but it depends on the truncation degree of the spherical harmonic expansion, ℓ_{max}, and on the grid discretization, since its dimension is $n_{point} \times n_{coef}$, where $n_{coef} = \ell_{max}(\ell_{max}+2)$. It also depends on the normalization used for f_ℓ^m. As for matrix $\mathbf{S}$, with dimension $n_{epoch} \times n_{coef}$, each of its columns is the set of values of the expansion coefficient s_ℓ^m at all n_{epoch} times and, like $\mathbf{F}$, it depends on the normalization.

Applying EOFA to matrix $\mathbf{S}$ means to project it onto matrix $\mathbf{Q}$ of eigenvectors of $\mathbf{C}_S = \mathbf{S}^T\mathbf{S}$, i.e., computing $\mathbf{Z} = \mathbf{S}\mathbf{Q}$ such that $\mathbf{Z}^T\mathbf{Z} = \Lambda_S$ is diagonal. $\mathbf{Q}$ is orthogonal, since it diagonalizes the real symmetric matrix $\mathbf{C}_S$. The EOFs are now the columns of $\mathbf{Q}$, and the columns of $\mathbf{Z}$ are the PCs multiplied by the corresponding singular values of $\mathbf{S}$ (or square roots of the eigenvalues of $\mathbf{C}_S$). Different $\lambda_{S,i}$ values squared can be found as elements of the diagonal matrix Λ_S, ordered from the larger to the smaller. The original matrix $\mathbf{S}$ can be written as a EOFA decomposition:

$$\mathbf{S} = \mathbf{Z}\mathbf{Q}^T . \tag{7}$$

One of the main purposes in this study is to clarify the relation between the EOFA modes retrieved from data matrix $\mathbf{S}$ and from $\mathbf{X}$. In fact, the transformation of different $\mathbf{S}$-EOFs using matrix $\mathbf{F}$ (see (6)) does not retrieve the $\mathbf{X}$-EOFs, as will be shown in the following. A unique definition of each mode is important, if a physical interpretation in terms of the underlying sources is sought. This will be the subject of the following section.

3. Concurrent EOFA Modes in the Spectral Domain and in the Spatial Grid

Using the notation introduced above, the eigenvector/eigenvalue equation for the covariance matrix $\mathbf{C}_X$ yields

$$\mathbf{C}_X\mathbf{P} = \mathbf{P}\Lambda_X . \tag{8}$$

From (6) and (7) and by the definition of Λ_S it can also be written as

$$\mathbf{C}_X = \mathbf{X}^T\mathbf{X} = \mathbf{FS}^T\mathbf{SF}^T = \mathbf{FQZ}^T\mathbf{ZQ}^T\mathbf{F}^T = \mathbf{FQ}\,\Lambda_S\,\mathbf{Q}^T\mathbf{F}^T \ . \tag{9}$$

If matrix $\mathbf{FQ}$ has the semiorthogonality property $(\mathbf{FQ})^T\mathbf{FQ} = \mathbf{I}$, then it is possible to identify in $\mathbf{FQ}$ a subspace of the eigenvectors of $\mathbf{C}_X$, with corresponding eigenvalues in Λ_S. Since $\mathbf{Q}$ is orthogonal, this can be achieved if $\mathbf{F}^T\mathbf{F} = \mathbf{I}$, which clearly is not the case, from the definition of matrix $\mathbf{F}$. A different transformation matrix $\mathbf{F}'$ can be introduced that satisfies the semiorthogonality relation $\mathbf{F}'^T\mathbf{F}' = \mathbf{I}$ and, through an equation analogous to (9), makes explicit the transformation rules between EOFA modes on SH coefficients and EOFA modes on a spatial grid.

Let the space-time data matrix $\mathbf{X}$ be transformed into

$$\mathbf{X}' = \mathbf{XG}^T \tag{10}$$

and the SH coefficients-time matrix $\mathbf{S}$ be transformed into

$$\mathbf{S}' = \mathbf{SN}^T \ , \tag{11}$$

where $\mathbf{G}$ and $\mathbf{N}$ are matrices that compensate for the overrepresentation of higher latitudes in a regular spatial grid and for a non–full normalization of spherical harmonics, respectively. These matrices are defined in Appendix A.

From equations (6) and (10), $\mathbf{X}' = \mathbf{SN}^T(\mathbf{N}^{-1})^T\mathbf{F}^T\mathbf{G}^T$, and by defining $\mathbf{F}'^T \equiv (\mathbf{N}^{-1})^T\mathbf{F}^T\mathbf{G}^T$, then

$$\mathbf{X}' = \mathbf{S}'\mathbf{F}'^T \ . \tag{12}$$

An important difference comparing to (6) is that $\mathbf{F}'$, as shown in Appendix A (see (A7)), is now a semiorthogonal matrix:

$$\mathbf{F}'^T\mathbf{F}' = \mathbf{I} \ . \tag{13}$$

Denoting by $\mathbf{Y}'$ and $\mathbf{P}'$ the matrices of PCs and EOFs of transformed data matrix $\mathbf{X}'$, the eigenvector/eigenvalue equation for the covariance matrix $\mathbf{C}_{X'}$ yields

$$\mathbf{X}'^T\mathbf{X}'\mathbf{P}' = \mathbf{P}'\Lambda_{X'} \tag{14}$$

where $\Lambda_{X'}$ is the diagonal matrix of eigenvalues of $\mathbf{C}_{X'}$. On the other hand, applying the EOF analysis to the transformed coefficient matrix $\mathbf{S}'$ gives $\mathbf{Z}'$ and $\mathbf{Q}'$ as the corresponding matrices of PCs and EOFs, respectively, meaning that $\mathbf{S}' = \mathbf{Z}'\mathbf{Q}'^T$. The transformation from spectral to spatial domain can then be written as $\mathbf{X}' = \mathbf{Z}'\mathbf{Q}'^T\mathbf{F}'^T$ (see (12)) leading to

$$\mathbf{X}'^T\mathbf{X}'(\mathbf{F}'\mathbf{Q}') = (\mathbf{F}'\mathbf{Q}')\Lambda_{S'} \tag{15}$$

where $\Lambda_{S'}$ is the diagonal matrix of eigenvalues of $\mathbf{C}_{S'} = \mathbf{S}'^T\mathbf{S}'$. Although $\mathbf{P}'$ and $\mathbf{F}'\mathbf{Q}'$ are different matrices, the former having $n_{point} \times n_{point}$ dimension and the later $n_{point} \times n_{coef}$, both (14) and (15) represent eigenvector/eigenvalue equations for the covariance matrix $\mathbf{C}'_X = \mathbf{X}'^T\mathbf{X}'$. As the eigenvector norms in both equations are set to 1 (since $\mathbf{P}'^T\mathbf{P}' = \mathbf{I}$ and $(\mathbf{F}'\mathbf{Q}')^T(\mathbf{F}'\mathbf{Q}') = \mathbf{I}$), common eigenvector/eigenvalue equations are represented in both cases. By construction, $\mathbf{P}'$ contains all eigenvectors of $\mathbf{C}_{X'}$ and $\Lambda_{X'}$ contains all eigenvalues. This is not the case for $\mathbf{F}'\mathbf{Q}'$ and $\Lambda'_{S'}$, if $n_{coef} < n_{point}$. However, as long as eigenvectors and eigenvalues are ordered by decreasing fraction of explained variance (see (1)) as matrix columns and diagonal values, and, by construction, the more relevant EOFA modes are included, we can guarantee correspondence between the first (main) ones. This has been checked numerically for the illustrative application in section 4, using the CM4 model.

The possibility of identifying the first columns of $\mathbf{P}'$ and $\mathbf{F}'\mathbf{Q}'$ relies heavily on the accuracy with which condition (13) is met. This problem is discussed in the scope of regular spatial grids (Appendix A) and irregular grids of Gauss-Legendre quadrature points (Appendix B). As shown in those appendices, the condition of semiorthogonality is met within a small error $\sim 10^{-4}$ with regular grids of a relatively small dimension and can be very substantially reduced to machine precision, i.e., to values $\sim 10^{-15}$, if one uses Gauss-Legendre grids for the polar angle.

Finally, also note that the EOF spatial patterns in columns of $\mathbf{P}$ can always be expanded in the basis of spherical harmonic functions f_ℓ^m such that $\mathbf{P}^T = \mathbf{R}^T\mathbf{F}^T$, where each column of matrix $\mathbf{R}$ contains the SH coefficients in the expansion of each corresponding column of matrix $\mathbf{P}$. Then, from (2), $\mathbf{X} = \mathbf{Y}\mathbf{R}^T\mathbf{F}^T$ and, from (6), $\mathbf{S} = \mathbf{Y}\mathbf{R}^T$ (as long as $\mathbf{F}^T$ has a right inverse). This is how the EOFA modes on the spatial grid are transposed to the SH domain in previous studies [e.g., *Langel*, 1987], with each spatial pattern found for $\mathbf{X}$ directly projected on the basis of spherical harmonic functions and multiplied by the time evolution given by the columns of $\mathbf{Y}$. However, from $\mathbf{S}^T\mathbf{S} = \mathbf{R}\mathbf{Y}^T\mathbf{Y}\mathbf{R}^T = \mathbf{R}\Lambda_X\mathbf{R}^T$, it can be realized that this is not an expansion in terms of EOFA modes for $\mathbf{S}$, since $\mathbf{R}^T\mathbf{R} \neq \mathbf{I}$ and as a result columns of $\mathbf{R}$ are not eigenvectors of the covariance matrix $\mathbf{C}_S$.

The procedure of how to apply the EOF analysis on the SH coefficients-time matrix in order to obtain (i) norm-independent modes and (ii) modes that are also modes of the (latitude weighted) grid when transformed to the space domain through (12) is now well established. As a summary, after transformation of $\mathbf{S}$ into $\mathbf{S}'$ which delivers a SH coefficient matrix independent of normalization, an eigenvector/eigenvalue problem is solved for covariance matrix $\mathbf{C}_{S'}$ giving matrices $\mathbf{Z}'$, $\mathbf{Q}'$, and $\Lambda_{S'}$. The concurrent modes in the spatial domain are identified as follows: the time-dependent amplitudes (PCs) of each coherent spatial structure are found in the first columns of matrix $\mathbf{Z}'$ (since first columns of $\mathbf{Y}'$ and of $\mathbf{Z}'$ are the same); the main coherent spatial structures (EOFs) are retrieved in the first columns of $\mathbf{F}'\mathbf{Q}'$; and the corresponding percentage of data variance explained is obtained from the first diagonal elements of $\Lambda_{S'}$.

4. Application to Geomagnetic Field Models

The main expression of temporal variability of the recent geomagnetic field, as observed at the Earth's surface, is found in the westward drift of the nondipole field and in the decay of the geomagnetic dipole moment. Although a global drift of around $0.2°$ yr^{-1} is often invoked, the westward drift shows important spatial variations changing in time [*Finlay and Jackson*, 2003; *Dumberry and Finlay*, 2007]. The geomagnetic dipole moment decay, mainly concentrated on the axial component, has been monitored since the first measurements of the geomagnetic field intensity by Gauss. Since 1840, the decrease is about 9% of the initial value, using *gufm1* and COV-OBS geomagnetic field models for the observatory era period [e.g., *Jackson et al.*, 2000; *Gillet et al.*, 2013]. As noticed by *Finlay et al.* [2012], changes in different morphology features combine to produce the current dipole decay, from growth and southward motion of reversed flux patches in the Southern Hemisphere [*Gubbins and Bloxham*, 1987] to weakening and equatorward flux transport of high-latitude normal flux lobes [*Olson and Amit*, 2006]. None of these main variability features (westward drift or axial dipole decay) can be simply described as a coherent structure evolving in time.

4.1. Geomagnetic Jerks as Coherent Structures Evolving in Time

Analysis of the geomagnetic secular acceleration (SA) over historical time periods brought out a few time-space events that are particularly interesting for EOFA application, since they can be described as a sequence of positive and negative pulses associated to the same spatial structure. *Le Huy et al.* [1998, 2000] first noticed a striking similarity between the acceleration maps at the Earth's surface computed for 1969, 1979, and 1992 epochs from observatory data and conjectured on possible implications for the surface core flow. These are dates at which global jerks, i.e., jumps of the secular acceleration corresponding to changes in the algebraic sign of the linear trend of the secular variation, occurring in less than 1 year, were reported [e.g., *Mandea et al.*, 2010]. Recently, *Chulliat and Maus* [2014] identified another similar space-time feature of the SA in more recent years, where a spatial structure comprising the low-latitude Atlantic sector and the Indian Ocean sector is seen to be coherently evolving at the core-mantle boundary, with abrupt changes in sign at 2003, 2007, and 2011. They further pointed out the interest of using EOFA to characterize such a feature.

Since the three jerks of 1969, 1979, and 1992 are predicted by the CM4 model [*Sabaka et al.*, 2004], we chose to apply our findings to this set of spherical harmonic coefficients and to evaluate, for this particular and well-known sequence of jerks, the relevance of the correction that we propose.

4.2. Results for SA Modes in CM4

The SA SH coefficients from CM4 model for the 1960–2002 period were inspected for main principal modes. Due to regularizations applied in the inversion for the CM4 model, the SA is resolved spatially only up to degree ~5–6 [e.g., *Gillet et al.*, 2010] and we use $\ell_{max} = 5$. As to the time evolution, the CM4 model uses order 4 splines with 2.5 years knot spacing, and it is therefore expected a temporal resolution of approximately the same value [see *Olsen et al.*, 2009]. We use a 1 year time sampling, keeping in mind that the computed

Table 2. Comparing Results Obtained Using a Regular Grid 3° × 3° Corresponding to $n_{point} = 1800$ (λ_X^{reg} and $\lambda_{X'}^{reg}$) and the Optimal Grid of Gauss-Legendre Quadrature Points for $\ell_{max} = 5$ (λ_X^{GL} and $\lambda_{X'}^{GL}$)

Modes	$\dfrac{|\lambda_X^{reg} - \lambda_{X'}^{GL}|}{\lambda_{X'}^{GL}}$ (%)	$\dfrac{|\lambda_X^{GL} - \lambda_{X'}^{GL}|}{\lambda_{X'}^{GL}}$ (%)	$\dfrac{|\lambda_{X'}^{reg} - \lambda_{X'}^{GL}|}{\lambda_{X'}^{GL}}$ (%)
1	12.9	9.7	0.03
2	11.2	8.2	0.07
3	7.2	3.2	0.05
4	4.1	3.1	0.07
5	1.6	1.3	0.05

modes may have a still lower temporal resolution. The number of epochs is then $n_{epoch} = 43$. Four sets of modes were computed and compared among themselves: modes from a matrix **S** filled with the CM4 SH coefficients at different epochs; modes from matrix **X**, a regular grid of the geomagnetic potential obtained from **S** according to equation (6); and modes from transformed matrix **X'** and from transformed matrix **S'**, obtained using equations (10) and (11), respectively. The transformation matrix **F** was computed for an optimal grid of Gauss-Legendre quadrature points corresponding to $\ell_{max} = 5$, implying $n_{point} = (2\ell_{max} + 1)(\ell_{max} + 1) = 66$ (Appendix B). Condition (A7) then holds within an error $\sim 10^{-15}$. All computations were repeated using also **F** for a regular grid 3° × 3° corresponding to $n_{point} = 1800$, for which condition (A7) holds within a still relatively small error $\sim 10^{-4}$. As shown in Table 2, differences are very small when comparing EOFA over transformed matrices **X'** (column 4) and are due uniquely to the fact that the semiorthogonality condition is verified more closely in one case than in the other. Comparing columns 2 and 3, we note a more interesting result, namely, that by applying EOF analysis to a raw **X** matrix of Gauss-Legendre quadrature points, the main principal modes are closer to those obtained from transformed matrices than if we had used a raw **X** of grid points distributed regularly in latitude and in longitude.

Figure 1 shows values of the fraction of variability f_i explained by each mode (see (1)) as obtained from Λ_S, $\Lambda_{S'}$, Λ_X, and $\Lambda_{X'}$. Only the 10 main modes are shown, which together comprise more than 90% of the total variability of corresponding data matrices. Although there can be modes for which f_i does not change significantly according to the data on which EOFA is applied (e.g., mode 3), in most cases the differences are significant. Largest differences are seen precisely for the first principal mode of SA. In general, those differences occur with no systematic pattern: the variability explained by a certain mode computed from Λ_X can be higher or smaller than when computed from Λ_S. However, when comparing corresponding modes computed from matrices $\Lambda_{S'}$ and $\Lambda_{X'}$, their variability fractions are always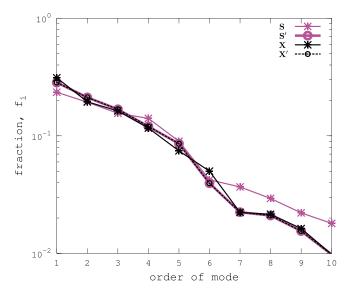 the same, as expected. These coincident estimated values can be very close to those obtained from Λ_S (e.g., modes 5 and 6) or from Λ_X (e.g., modes 4 and 7–9), but again, no systematic behavior is found.

Differences in the time variation associated to each mode are shown in Figure 2. In Figure 2a (left), curves of the same color represent the normalized PCs when working directly on data matrices **S** and **X**, i.e., columns of matrix **Y** divided by the singular values $\lambda_{X,i}$ (dotted curves with markers) and columns of **Z** divided by corresponding $\lambda_{S,i}$ (solid lines) (see also (3)). As we can see, they are, in general, quite distinct. Corresponding plots in Figure 2a (right) show that the normalized PCs from a similar analysis on **X'** and **S'** do superpose perfectly. In general,

Figure 1. Fraction of variability using equation (1), for the 10 first modes obtained when applying EOFA to matrices **X**, **S**, **X'**, and **S'** (see text).
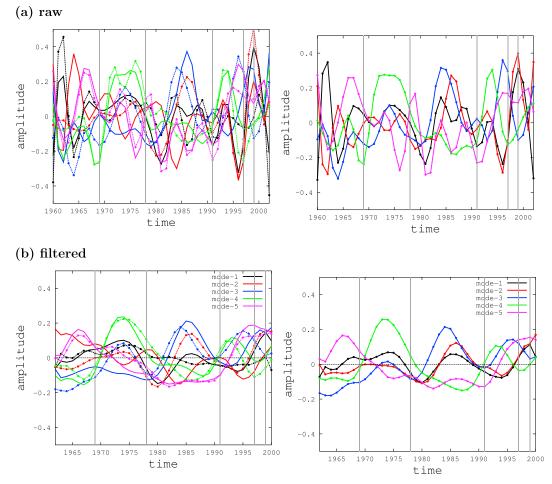
(a) raw

(b) filtered

Figure 2. First five main PCs for SA-CM4, using EOFA on different data matrices: matrices **S** (solid) and **X** (dotted) on the left column and transformed matrices **S′** (solid) and **X′** (dotted) on the right column. Curves obtained (a) from raw application of EOFA and (b) using a filter on raw PCs, as explained in the text. Shown are mode 1 (black), mode 2 (red), mode 3 (blue), mode 4 (green), and mode 5 (magenta).

the time variation recovered for each mode depends significantly on which data matrix is used in the EOF analysis, except when comparing results from transformed matrices **S′** and **X′**.

Curves in Figure 2a are quite irregular. A filter was applied to eliminate oscillations caused by the finite model temporal resolution related to splines' knot spacing of 2.5 years but still preserve step edges which are important to localize epochs of sign changes. The applied operator is a combination of a median filter of length 3 years to eliminate spikes, followed by a moving average of width 5 years in order to smooth the signal. The role of the 2.5 years knot spacing in limiting the effective temporal resolution is quite clear in the number of nonnegligible singular values of any of the data matrices. This value amounts to 17, the rounded down integer of $n_{epoch}/2.5$. Oscillations of period ≤ 5 years then risk to be due to an aliasing effect. Filtered curves are represented in Figure 2b. Again, a distinct behavior of curves of the same color and different markers is seen on the left, while on the right curves of the same color superpose exactly.

Figure 3 shows charts for the three vector components obtained from the EOFs of orders 3 (Figure 3b) and 4 (Figure 3a) for the $\ddot{V}$ geomagnetic potential (see (3)), through $\ddot{\mathbf{B}} = -\nabla\ddot{V}$.

4.3. Results for SV and MF Modes in CM4

We further considered EOFA modes obtained from secular variation (SV) and main field (MF) SH coefficients of the CM4 model, truncated at degree $\ell_{max} = 5$. Figure 4 shows the fraction of variability f_i for the 10 main modes of (a) SV and (b) MF. The relative importance of each mode decreases with the order number more quickly for the SV modes than for SA and still more abruptly for the MF modes where the first mode alone explains more than 90% of the whole variability. Differences resulting from using **S** and **X** instead of **S′** and
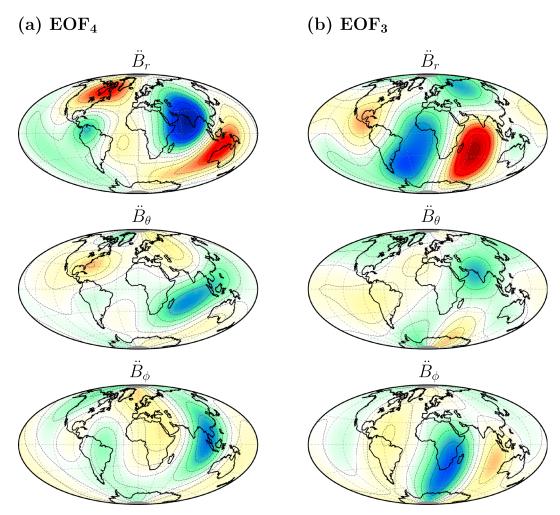
(a) $\mathbf{EOF_4}$ (b) $\mathbf{EOF_3}$

Figure 3. Vector components of (a) SA-EOF$_4$ and (b) SA-EOF$_3$, as computed from CM4. Algebraic sign in agreement with signs of corresponding PCs in Figure 2, so that $(\mathbf{PC})_i\,(\mathbf{EOF})_i^T$ (equation (3)) gives the correct sign for the contribution of mode i to potential $\ddot{V}$. Relative amplitudes between different components for the same mode were preserved.

$\mathbf{X}'$ are small for the two first principal modes in both SV and MF. While for the MF signal these two modes alone explain almost all the variability, for the SV signal there is still a nonnegligible contribution from modes 3 and 4, amounting to about 5%. It is thus important to acknowledge that the PCs for modes 3 and 4 depend strongly on which data matrix is used, as shown in Figure 5a. The degree of degeneracy existing between the two modes may contribute to this result (see Figure 4a), by promoting a different separation between them each time a different transformation is applied on the total SV signal.

5. Discussion

Since, as generally accepted, jerks are an expression of the Earth's core dynamics, looking for them in the core internal component of comprehensive models such as CM4 is most convenient. It provides a time-dependent internal component cleaned up from external and induced fields, which are prone to degrade the signal [e.g., *Sabaka et al.*, 2004].

5.1. SA Mode 4: Reproducing a Known Sequence of Jerks

Grey vertical lines in Figure 2 show the most often given epochs for the sequence of impulsive-type global events identified during the CM4 time interval 1960–2002, namely, the 1969, 1978, and 1991 jerks [e.g., *Le Huy et al.*, 1998; *Mandea et al.*, 2010], the 1997 jerk pointed out in *Sabaka et al.* [2004], and the 1999 jerk pointed out by *Mandea and Macmillan* [2000]. In Figure 2a (right), mode 4 (green curve; see legend) stands out as having a temporal behavior that more nearly sticks to a mode possibly describing the five referred jerks, i.e., showing
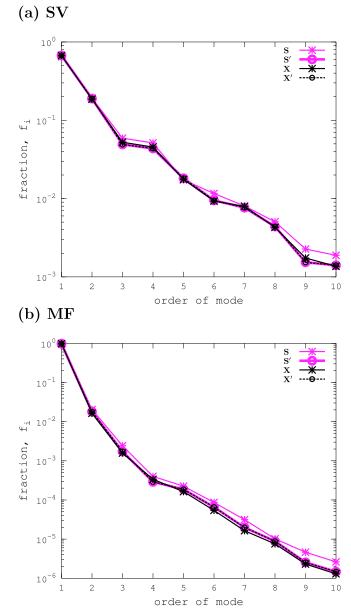
(a) SV

(b) MF

Figure 4. Fraction of variability using equation (1), for the 10 first modes obtained when applying EOFA to matrices **X**, **S**, **X′**, and **S′** of (a) SV and (b) MF.

relatively abrupt and high-amplitude changes of sign close to grey lines. The most significant changes of sign are preserved in filtered curves of Figure 2b (right) where they can still be seen very close to grey vertical lines.

Note that such a distinctive behavior has been made clearer due to an application of EOFA on transformed matrices; a scrutiny on jerk time occurrence using EOFA modes computed for matrix **X** would have given dates more close to 1981 and 1995 than to 1978 and 1997, respectively (Figure 2b, left).

The morphology of the three vector components of mode 4 (Figure 3a) is very similar to the charts of successive geomagnetic jerks of 1969, 1978, and 1991 at the Earth's surface obtained by *Le Huy et al.* [1998] (see their Figures 4–6), especially their 1969 and 1991 (which they set at 1992) charts. The strongest foci of $\ddot{B}_r$ flux over west of India, northwest of Australia, north of South America, and between Canada and Greenland do show strong correlation with corresponding foci in *Le Huy et al.* [1998] chart for 1969. Over South Atlantic, the correlation is higher with their 1992 charts. Charts in Figure 3a are also very similar to charts shown by *Sabaka et al.* [2004] (their Figure 9), when discussing the prediction of the most well-known jerks by the CM4 model, and by *Pinheiro et al.* [2011] after inverting amplitudes of first differences of annual observatory mean data
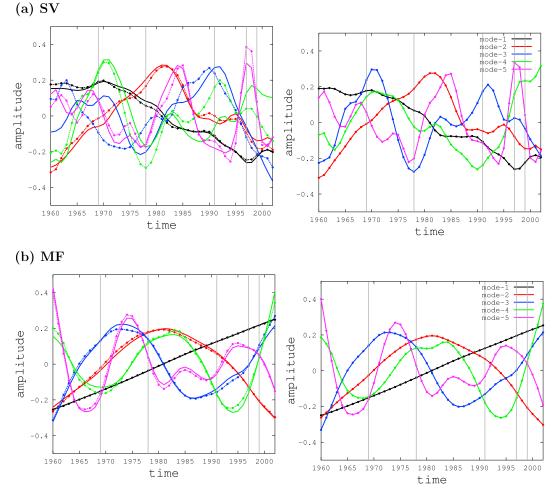
Figure 5. First five main PCs for (a) SV-CM4 and (b) MF-CM4, using EOFA on different data matrices: matrices **S** (solid) and **X** (dotted) on the left column and transformed matrices **S'** (solid) and **X'** (dotted) on the right column. Shown are mode 1 (black), mode 2 (red), mode 3 (blue), mode 4 (green), and mode 5 (magenta).

around the jerk occurrence times (their Figure 14). Again, the similarity is particularly strong with respect to the 1969 jerk.

While the EOF analysis here applied for the 1960–2002 period localizes the first jerk at 1970 rather than at 1969 (see Figure 2) and the third jerk at 1992 rather than at 1991, this 1 year difference may perfectly be due to the finite ~2 years temporal resolution of the CM4 model. Our EOF analysis further identifies relatively sudden variations in sign for mode 4 close to 1996 and 2000, supporting the suggestion of *Sabaka et al.* [2004] that events that they localize at 1997 and 2000 could be the follow up of the sequence initialized with the three first jerks.

As to the reason the spatial pattern of SA mode 4 has not been retrieved in more recent epochs, it might be that the recurrence time of this mode is relatively large and that some more time needs to pass before a clear observation of a new pulse can be done. To support this view, Figure 2 shows that the time interval between the two maxima of successive pulses of SA-PC_4 is about 20 years. Such a recurrence time would imply that a new pulse of this mode might be already present, although the time interval of data available could be insufficient for a precise retrieval. In fact, when applying EOF analysis to the CHAOS-5 SA model, an extension of CHAOS-4 model [*Olsen et al.*, 2014] spanning 1997.0 to 2015.0, and using the modified **S'** as explained in this study, we identify interesting features in SA mode 4. Its $\ddot{B}_r$ chart shows maximum flux spots close to Australia, India, and Canada, with similar structure to those in Figure 3a, in spite of some shift of the foci and the presence of further features possibly showing mixing with other modes (Figure 6). It may be the expression in CHAOS-5, of the same coherent structure represented by SA mode 4 in the CM4 model.
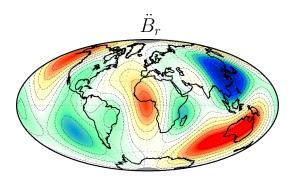
$$\ddot{B}_r$$

Figure 6. Chart of the radial component of normalized SA-EOF$_4$, obtained from CHAOS-5.

5.2. Application for Recovering the Flow That Generates SA Mode 4

From comparison of the left and right plots in Figure 5a, we notice that the effect of applying EOF analysis on matrices **X**′ and **S**′ modifies strongly the time series SV-PC$_3$ and SV-PC$_4$. Interestingly, a link between SV mode 3 and SA mode 4 becomes apparent: SV-PC$_3$ on the right plot clearly shows changes in trend sign at the same epochs when jumps in SA-PC$_4$ occur, namely, close to 1970, 1978, 1992, and 1996. An exception is the last jump around 2000 that does not find correspondence in SV-PC$_3$. Also, two further trend sign changes are present in SV-PC$_3$ that find no correspondence in SA-PC$_4$, in 1983 and 1986. These are epochs where jerks have been identified [e.g., *Brown et al.*, 2013]. Note that the 1983, 1986, and 1996 changes in trend sign show up as features of the same SV mode 3 only after EOF analysis has been applied to the modified matrices **X**′ and **S**′. Again, it should be stressed that a certain degree of degenerescence exists between SV-PC$_3$ and SV-PC$_4$ and that these two modes are probably never completely separated, whatever the data matrices in use, given the very close values of f_i [e.g., *Preisendorfer*, 1988]. The whole set of events around 1970, 1978, 1983, 1986, and 1992 is again present in MF-PC$_5$, at epochs of change in sign of curvature (Figure 5b). As can also be seen in Figure 5, the effect of using corrected data matrices is less important for the case of EOF analysis applied to the MF than for SV and SA.

Besides the fact that the PCs of SA mode 4, SV mode 3, and MF mode 5 can be very approximately recovered one from the other successively through time integration, their EOFs are strongly correlated as shown in Figure 7. Note that nonzero correlation values between spatial structures of different orders, shown in Figures 7a and 7b, are possible because the comparison is between principal modes from different data matrices (SA and SV or SA and MF, respectively). For a given signal, EOFs with different order are, by construction, orthogonal. In those plots, only correlation values above 0.65 are shown. Figures 7c and 7d are to be compared with top chart of Figure 3a. Focusing on the SV mode 3 chart, which is expected to be better retrieved than MF mode 5 (because of higher represented data variability), we notice strong foci of $\dot{B}_r$ localized over the same regions of Western India, northwest of Australia, and Eastern Canada, as was the case of $\ddot{B}_r$ foci for SA mode 4. The chart for SV mode 3 in Figure 7c further shares with corresponding chart for SA mode 4, a very faint expression of those modes over the South Atlantic region. Main differences are the stronger $\dot{B}_r$ focus over Colombia/Venezuela and, maybe more interestingly, the emergence of a new focus over the Pacific. This structure might be absent from the SA signal because of penalizing regularization effects that are stronger for SA than for SV.

The high correlation between SA mode 4 and SV mode 3 may be used to infer about the core surface flow which, by interaction with the main field, is generating SV mode 3. Our result, in fact, suggests that as proposed by *Le Huy et al.* [2000], such flow component may also be modeled as a standing feature characterized by a fixed spatial pattern evolving in time. This idea is also present in *Chulliat and Maus* [2014]. In both previous studies a simplified time evolution is considered for the flow, either a sequence of trends with sign change events at the time of jerks [*Le Huy et al.*, 1998] or a sinusoid with periodicity 6 years [*Chulliat and Maus*, 2014]. In this study, the retrieved SV mode 3 provides for a SV-PC$_3$ time series that gives the time evolution of the flow directly from the CM4 model and for a SV-EOF$_3$ pattern that can be inverted for the spatial structure of the flow.

5.3. SA Mode 3: Exposing a New Sequence of Known Jerks

One other mode, mode 3, attracted our attention for well-localized and high-amplitude changes in sign around 1982 and 1988, but also in 1994 and 1998, as shown in Figure 2a (right). They are still seen after filtering, except the sign change around 1998, possibly due to the proximity to the end of the analyzed time interval (Figure 2b, right). This mode accounts for an important fraction of data variability, above 10% (see Figure 1), thus calling for further inspection.
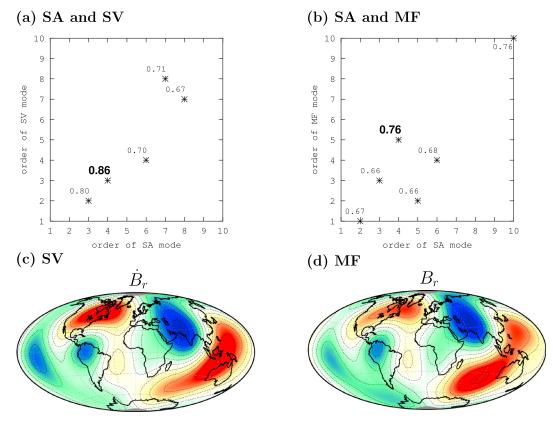
(a) SA and SV

(b) SA and MF

(c) SV

$\dot{B}_r$

(d) MF

B_r

Figure 7. For the first 10 EOFs of SA, SV, and MF, correlation values r above 0.65 between (a) SA and SV and (b) SA and MF. Values computed according to $r_{ij} = \mathbf{EOF}_i^T \mathbf{EOF}_j / \left(\sqrt{\mathbf{EOF}_i^T \mathbf{EOF}_i} \sqrt{\mathbf{EOF}_j^T \mathbf{EOF}_j} \right)$. Charts of the radial component of normalized (c) SV-EOF$_3$ and (d) MF-EOF$_5$.

This sequence of jerks, with a spatial pattern showing features over the Indian and South Atlantic Oceans (see Figure 3b), gets particularly active after 1980, with jerk-like events that can be associated to two pulses of the SA, around 1985 and 1996, using *Chulliat et al.* [2010] terminology. It is possible to identify jerks at the sequence of dates above, at some selected permanent observatories as, e.g., MBour (Senegal) and Pamatai (French Polynesia) [see, e.g., *Wardinski and Holme*, 2006]. Their global detection is difficult when comparing with the series of jerks of SA mode 4, and they tend to fail the robustness criteria of some jerk detection methods [e.g., *Brown et al.*, 2013]. However, an interesting point to notice is that studies on most recent jerks show that the same regions (low-latitude Atlantic sector and Indian Ocean sector) have felt pulses of SA during the last 20 years of continuous geomagnetic satellite missions, in 2006 and 2009, accompanied by geomagnetic jerks in 2003, 2007, and 2011 [*Lesur et al.*, 2008; *Chulliat et al.*, 2010; *Chulliat and Maus*, 2014]. We find correspondence, in particular, between the $\ddot{B}_r$ flux foci over southward of India and Gulf of Guinea in Figure 3b, with different signs between them, and features in recent geomagnetic field jerks computed by those authors at the Earth's surface. A possible explanation for an easier identification of this pattern in recent years is the great improvement brought by satellite missions for the spatial coverage over those regions, which lack magnetic observatories and repeat stations.

5.4. Computing SH Models of Coherent Structures From Data on a Grid

Another application of the present study on optimal grids to use and on the required transformations to apply in order to find concurrent principal modes in spatial and spectral domains is the use of EOFA directly on satellite data. By doing so, we can skip the fit of a spherical harmonic series first, followed by the EOFA applied to the set of SH coefficients [*Golovkov et al.*, 2005]. A spatial grid of Gauss-Legendre quadrature points is the natural grid to envisage given that (A7) is exact (to machine precision) in that case. Eventually, a temporal and spatial filtering of satellite data should be previously applied in filling this optimal grid with data values. In fact, at the light of results obtained here, it seems pertinent to reconsider the use of EOF data analysis tools in geomagnetic field modeling and to further test the original claim by *Pushkov et al.* [1976] and

Golovkov et al. [1978, 2005] that NOC could be useful in providing a nonparametric means of separating components due to internal and external sources and even components due to different magnetospheric or ionospheric current systems.

6. Conclusions

We show that EOFA modes of a set of time-dependent data sampled on a spatial grid should not be directly obtained from the EOFA modes of the corresponding set of SH Schmidt normalized coefficients. Instead, a preliminary transformation of the SH coefficients is required, to generate a norm-independent matrix. The PCs and eigenvalues then obtained are the same in the spectral domain and in the spatial domain modified by a certain weight matrix. We further identified the transformation that allows to retrieve the EOFs in the spatial domain.

An error is unavoidable when going from the exact description in terms of the original spherical harmonic models to the required approximation when generating a spatial grid. This error is reduced to the level of machine precision if one uses a spatial grid of Gauss-Legendre quadrature points for the polar angles, because the orthonormality relations of spherical harmonics are exactly fulfilled for this grid. In Appendices A and B the whole procedure is described in detail, for an easy implementation.

Using EOF as a data analysis tool on the CM4 internal field model, our SA mode 4 sequence of jerks recovers the spatial pattern retrieved in previous studies by *Le Huy et al.* [1998] [see also *Sabaka et al.*, 2004; *Pinheiro et al.*, 2011], with abrupt changes in sign at the time of the well-known jerks of 1969, 1978, and 1991. This shows that the method is most suited to characterize these kind of events, previously identified with very different and, in general, more thorough analysis, and important since the linking of different jerks to similar spatial structures may be of help in determining their origin.

An interesting unveiling of the SA mode 4 jerk-mode pattern in modes of CM4-SV and even CM4-MF models is a novelty from this study and opens new perspectives for dedicated studies to recover the "jerky" core flow. Another new result is the finding of a second sequence of jerks in SA mode 3, with a spatial pattern showing features over the Indian and South Atlantic Oceans, particularly active after 1980, corresponding to two pulses of SA around 1985 and 1996. Their spatial structure shows striking similarities with the spatial description of recent jerks occurred during the satellite era. Finally, we point out that the method can be used to produce spherical harmonic models of decorrelated modes, hopefully related to different sources, directly from a grid of data values.

Appendix A: Matrices of Grid Weight and SH Normalization

The coefficients of **F** are values of the spherical harmonics on a grid that covers the whole spherical surface. The expressions for $f_\ell^m(\theta, \phi)$ are

$$f_\ell^m(\theta, \phi) = C_\ell^m(\theta, \phi) = P_\ell^m(\theta) \cos m\phi, \text{ for } m = 0, 1, 2, ...$$

and

$$f_\ell^m(\theta, \phi) = S_\ell^m(\theta, \phi) = P_\ell^m(\theta) \sin m\phi, \text{ for } m = 1, 2, ... \quad (A1)$$

In the case of Schmidt quasi-normalization of surface spherical harmonics,

$$\frac{1}{4\pi} \int_0^{2\pi} \int_0^\pi C_\ell^m(\theta, \phi) C_{\ell'}^{m'}(\theta, \phi) \sin\theta \, d\theta \, d\phi = \frac{1}{2\ell + 1} \delta_\ell^{\ell'} \delta_m^{m'}$$

$$\frac{1}{4\pi} \int_0^{2\pi} \int_0^\pi S_\ell^m(\theta, \phi) S_{\ell'}^{m'}(\theta, \phi) \sin\theta \, d\theta \, d\phi = \frac{1}{2\ell + 1} \delta_\ell^{\ell'} \delta_m^{m'}$$

$$\frac{1}{4\pi} \int_0^{2\pi} \int_0^\pi C_\ell^m(\theta, \phi) S_{\ell'}^{m'}(\theta, \phi) \sin\theta \, d\theta \, d\phi = 0 . \quad (A2)$$

In the limit of an infinite number of grid points, the Riemann sums converge to the above integrals:

$$\lim_{\Delta\theta,\Delta\phi\to 0} \sum_{l=1}^{n_{\text{point}}} C_\ell^m(\theta_l,\phi_l) C_{\ell'}^{m'}(\theta_l,\phi_l)\,\sin\theta_l\,\Delta\theta\,\Delta\phi = \frac{4\pi}{2\ell+1}\delta_\ell^{\ell'}\delta_m^{m'}$$

$$\lim_{\Delta\theta,\Delta\phi\to 0} \sum_{l=1}^{n_{\text{point}}} S_\ell^m(\theta_l,\phi_l) S_{\ell'}^{m'}(\theta_l,\phi_l)\,\sin\theta_l\,\Delta\theta\,\Delta\phi = \frac{4\pi}{2\ell+1}\delta_\ell^{\ell'}\delta_m^{m'}$$

$$\lim_{\Delta\theta,\Delta\phi\to 0} \sum_{l=1}^{n_{\text{point}}} C_\ell^m(\theta_l,\phi_l) S_{\ell'}^{m'}(\theta_l,\phi_l)\,\sin\theta_l\,\Delta\theta\,\Delta\phi = 0\,. \tag{A3}$$

The set of all Riemann sums above can be written as

$$\lim_{\Delta\theta,\Delta\phi\to 0} \sum_{l=1}^{n_{\text{point}}} F_{li}F_{lj}\,\sin\theta_l\,\Delta\theta\Delta\phi = \frac{4\pi}{2\ell_i+1}\mathbf{I}_{ij} \tag{A4}$$

where $\mathbf{I}_{ij}$ is element (i,j) of the $n_{\text{coef}}\times n_{\text{coef}}$ identity matrix. This convergence can be tested by computing the matrix product $\mathbf{F}^T\mathbf{G}^T\mathbf{GF}$, where the grid matrix $\mathbf{G}$ is a diagonal matrix that depends only on the spatial grid (chosen points and discretization):

$$\mathbf{G} = \sqrt{\Delta\theta\Delta\phi}\begin{bmatrix} \sqrt{\sin\theta_1} & \cdots & \cdots & \cdots \\ \cdots & \sqrt{\sin\theta_2} & \cdots & \cdots \\ \vdots & \vdots & \vdots & \vdots \\ \cdots & \cdots & \cdots & \sqrt{\sin\theta_{n_{\text{point}}}} \end{bmatrix}. \tag{A5}$$

Note that the $\sqrt{\sin\theta}$ factor is often applied to a regular grid on a sphere, to compensate for the meridian convergence and consequent oversampling toward higher latitudes.

Another useful matrix is the normalization matrix $\mathbf{N}$, also diagonal:

$$\mathbf{N} = \sqrt{4\pi}\begin{bmatrix} \sqrt{\frac{1}{2\ell_1+1}} & \cdots & \cdots & \cdots \\ \cdots & \sqrt{\frac{1}{2\ell_2+1}} & \cdots & \cdots \\ \vdots & \vdots & \vdots & \vdots \\ \cdots & \cdots & \cdots & \sqrt{\frac{1}{2\ell_{n_{\text{coef}}}+1}} \end{bmatrix}. \tag{A6}$$

Its elements depend only on the used normalization for spherical harmonic functions, which in geomagnetism is commonly the Schmidt quasi-normalization. For a full normalization as that used in gravimetry this matrix would have a simpler form; it would be the identity matrix multiplied by some constant.

From equation (A4), the following matrix equality will be verified for a dense spatial grid :

$$(\mathbf{N}^{-1})^T\mathbf{F}^T\mathbf{G}^T\mathbf{GFN}^{-1} = \mathbf{F}'^T\mathbf{F}' = \mathbf{I}\,, \tag{A7}$$

where matrix $\mathbf{F}' = \mathbf{GFN}^{-1}$ is introduced for simplicity. How dense the spatial grid must be so that equation (A7) is met within an acceptable error is shown in Figure A1, where deviations are plotted as a function of the grid discretization.
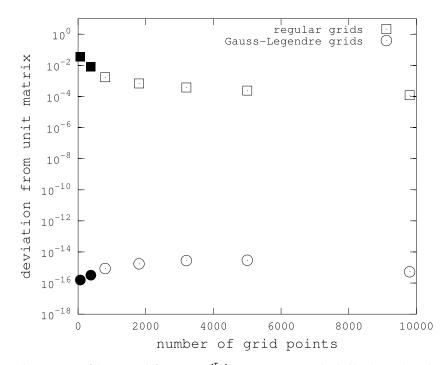
Figure A1. Frobenius norm of the matrix difference $\mathbf{I} - \mathbf{F'}^T\mathbf{F'}$ (see equation (A7)) divided by the total number of SH coefficients, as a function of total number of grid points (n_{point}), when using grid weights given by (A5) (squares) or by (B6) (circles). Empty squares are for regular grids with $\Delta\theta = \Delta\phi$. Empty circles are for nonregular grids of Gauss-Legendre quadrature points, with the same n_{point} values as empty squares. Filled black circles are for optimal grids of Gauss-Legendre quadrature points with $\ell_{\max} = 5$ (lower value) and $\ell_{\max} = 13$ (higher value). Filled black squares are for regular grids with $\Delta\theta \neq \Delta\phi$ and the same n_{point} values as filled black circles.

A regular grid is not, however, the most judicious grid to use in search for a more precise fulfillment of the (A7) relation. Appendix B shows how a grid built from Gauss-Legendre quadrature points is better to achieve this goal.

Appendix B: Optimal Choice of the Space Grid

For the sums in (A3), let us consider a grid $n_{\text{point}} = n_\theta \times n_\phi$ where n_θ and n_ϕ are, respectively, the number of values for θ and ϕ. Because the functions C_ℓ^m and S_ℓ^m in (A1) are products of functions of θ and ϕ, we can perform separately the respective sums. We will now show how, if the space grid and weights for each point are properly chosen, the orthonormality relations in (A3) hold *exactly* for a finite grid, i.e.,

$$\sum_{j=1}^{n_\theta} \sum_{i=1}^{n_\phi} C_\ell^m(\theta_j, \phi_i) C_{\ell'}^{m'}(\theta_j, \phi_i)\, w(\theta)_j\, w(\phi)_i = \frac{4\pi}{2\ell+1}\, \delta_\ell^{\ell'}\, \delta_m^{m'}$$

$$\sum_{j=1}^{n_\theta} \sum_{i=1}^{n_\phi} S_\ell^m(\theta_j, \phi_i) S_{\ell'}^{m'}(\theta_j, \phi_i)\, w(\theta)_j\, w(\phi)_i = \frac{4\pi}{2\ell+1}\, \delta_\ell^{\ell'}\, \delta_m^{m'}$$

$$\sum_{j=1}^{n_\theta} \sum_{i=1}^{n_\phi} C_\ell^m(\theta_j, \phi_i) S_{\ell'}^{m'}(\theta_j, \phi_i)\, w(\theta)_j\, w(\phi)_i = 0 \,, \tag{B1}$$

where $w(\theta)_j$ and $w(\phi)_i$ are the weights for each grid point j, i.

B1. Grid in ϕ

We choose a uniform grid for the values ϕ_i, with $w(\phi)_i = \Delta\phi$ for any i, such that $\phi_i = i\,\Delta\phi$, $i = 0, \dots, n_\phi - 1$, and $\Delta\phi = 2\pi/n_\phi$. The three types of sums over the functions of angles ϕ_i in (B1), with an index shift, are

$$\sum_{i=0}^{n_\phi - 1} \cos(m\,i\,\Delta\phi)\cos(m'\,i\,\Delta\phi)\Delta\phi = \sum_{i=0}^{n_\phi - 1} \left\{ \cos[(m-m')\,i\,\Delta\phi] + \cos[(m'+m)\,i\,\Delta\phi] \right\} \Delta\phi/2$$

$$\sum_{i=0}^{n_\phi - 1} \sin(m\,i\,\Delta\phi)\sin(m'\,i\,\Delta\phi)\Delta\phi = \sum_{i=0}^{n_\phi - 1} \left\{ \cos[(m-m')\,i\,\Delta\phi] - \cos[(m'+m)\,i\,\Delta\phi] \right\} \Delta\phi/2$$

$$\sum_{i=0}^{n_\phi - 1} \cos(m\,i\,\Delta\phi)\sin(m'\,i\,\Delta\phi)\Delta\phi = \sum_{i=0}^{n_\phi - 1} \left\{ \sin[(m'-m)\,i\,\Delta\phi] + \sin[(m'+m)\,i\,\Delta\phi] \right\} \Delta\phi/2 . \tag{B2}$$

In equation (B2) the sums are of the general form $\sum_i \cos(k\,i\,\Delta\phi)$ and $\sum_i \sin(k\,i\,\Delta\phi)$, $0 \leq |k| \leq 2\ell_{max}$. If we set the maximum value of $\Delta\phi$ to $2\pi/(2\ell_{max} + 1)$, i.e., the minimum value of n_ϕ equal to $2\ell_{max} + 1$, one can show that the sums above will be all zero for any values of m, m' with $m \neq m'$, i.e., $1 \leq |k| \leq 2\ell_{max} - 1$, and also for $k = 2\ell_{max}$. For $n_\phi \leq 2\ell_{max}$ this is no longer the case.

The third sum is also zero when $m = m'$. For $m = m' \neq 0$, the first and second sums are equal to $n_\phi \Delta\phi/2 = \pi$. For $m = m' = 0$, one gets 2π for the first sum and zero for the second one.

In conclusion, if we choose a uniform grid in ϕ with $\phi = 0, \Delta\phi, \dots, 2\pi - \Delta\phi$, with $\Delta\phi = 2\pi/n_\phi$ and at least $n_\phi = 2\ell_{max} + 1$, the sum over ϕ values assures that the third equation in (B1) is satisfied and we get for the first and second equations the contribution $\pi\delta_m^{m'}$ ($m \neq 0$) in their right-hand sides and for the first one $2\pi\delta_m^{m'}$ ($m = 0$).

B2. Grid in θ

For the sums in θ values, we first note that the associated Legendre polynomials $P_\ell^m(\theta)$ in C_ℓ^m and S_ℓ^m are polynomials of $\cos\theta$ and $\sin\theta$. From their definition in terms of the Legendre polynomials $P_\ell(\theta)$, which are polynomials of degree ℓ in $\cos\theta$ [*Abramowitz and Stegun*, 1965], the terms of the polynomials have the general form $a_k\,(\cos\theta)^{\ell-2k-m}(\sin\theta)^m$, $k = 0, 1, \dots, [(\ell-m)/2]$, where a_k are constant coefficients and $[(\ell-m)/2]$ is the largest integer equal or less than $(\ell-m)/2$. Thus, the term with the highest power of $\cos\theta$ is proportional to $(\cos\theta)^{\ell-m}(\sin\theta)^m$.

If we perform first the sum in ϕ in (B1), the nonzero terms involve products of associated Legendre polynomials with the same m, i.e.,

$$P_\ell^m(\theta_j)\,P_{\ell'}^m(\theta_j) \propto (\cos\theta_j)^{\ell+\ell'-2m}(\sin\theta_j)^{2m} + \dots \propto (\cos\theta_j)^{\ell+\ell'} + \dots$$

where only the term with the highest power in $\cos\theta$ is shown. This means that the product $P_\ell^m(\theta_j)\,P_{\ell'}^m(\theta_j)$ is a polynomial in $\cos\theta_j$ of degree $\ell + \ell'$.

We recall that the sums in (B1) were introduced to implement in matrix form the orthonormality relations (A2). Rewriting the integrals in θ in terms of $x = \cos\theta$

$$\int_0^\pi P_\ell^m(\theta)\,P_{\ell'}^m(\theta)\,\sin\theta\,d\theta = \int_{-1}^1 P_\ell^m(x)\,P_{\ell'}^m(x)\,dx , \tag{B3}$$

we see that what we want to write as a finite sum is the integral of a polynomial in x with degree $\ell + \ell'$. It so happens that Gaussian quadrature is exact for precisely this type of integral [*Abramowitz and Stegun*, 1965]. In particular, if $f(x)$ is a polynomial in x of degree $2n - 1$ or less, we apply n point Gauss-Legendre quadrature to yield the following equality:

$$\int_{-1}^1 f(x)\,dx = \sum_{i=1}^n w_i\,f(x_i) , \tag{B4}$$

where x_i are the n zeros of the Legendre polynomials $P_n(x)$ and $w_i = 2/\{(1 - x_i^2)[P_n'(x_i)]^2\}$ the positive weights. Since the maximum value for $\ell + \ell'$ is $2\ell_{max}$, we have to consider at least $n_\theta = \ell_{max} + 1$ terms in the sum for the quadrature formulas.

The sums in θ are then written in terms of $x_j = \cos\theta_j$, zeros of the Legendre polynomials $P_{n_\theta}(x)$,

$$\int_{-1}^{1} P_\ell^m(x)\,P_{\ell'}^m(x)\,\mathrm{d}x = \sum_{i=1}^{n_\theta} w_i\,P_\ell^m(x_i)\,P_{\ell'}^m(x_i)$$

where $n_\theta \geq \ell_{\max} + 1$.

Since for the Schmidt quasi-normalization of Legendre-associated polynomials one has

$$\int_{-1}^{1} P_\ell^m(x)\,P_{\ell'}^m(x)\,\mathrm{d}x = \begin{cases} \frac{2}{2\ell+1}\delta_\ell^{\ell'}\,, & m = 0 \\ \frac{4}{2\ell+1}\delta_\ell^{\ell'}\,, & m \neq 0 \end{cases}$$

we can write finally, as *exact* formulas

$$\sum_{j=1}^{n_\theta}\sum_{i=0}^{n_\phi-1} C_\ell^m(\theta_j,\phi_i)C_{\ell'}^{m'}(\theta_j,\phi_i)\,w_j\,\Delta\phi = \frac{4\pi}{2\ell+1}\delta_\ell^{\ell'}\,\delta_m^{m'}$$

$$\sum_{j=1}^{n_\theta}\sum_{i=0}^{n_\phi-1} S_\ell^m(\theta_j,\phi_i)S_{\ell'}^{m'}(\theta_j,\phi_i)\,w_j\,\Delta\phi = \frac{4\pi}{2\ell+1}\delta_\ell^{\ell'}\,\delta_m^{m'}$$

$$\sum_{j=1}^{n_\theta}\sum_{i=0}^{n_\phi-1} C_\ell^m(\theta_j,\phi_i)S_{\ell'}^{m'}(\theta_j,\phi_i)\,w_j\,\Delta\phi = 0 \,, \tag{B5}$$

with ϕ_i, θ_j, w_j, $\Delta\phi$, n_ϕ and n_θ defined as above.

The diagonal matrix **G** (A5) becomes for this grid

$$\mathbf{G} = \sqrt{\Delta\phi}\begin{bmatrix} \sqrt{w_1} & \cdots & \cdots & \cdots \\ \cdots & \sqrt{w_2} & \cdots & \cdots \\ \vdots & \vdots & \vdots & \vdots \\ \cdots & \cdots & \cdots & \sqrt{w_{n_{\text{point}}}} \end{bmatrix}, \tag{B6}$$

where w_k $(k = 1, \ldots, n_{\text{point}})$ have weight values corresponding to the particular point j of the θ grid.

By using a Gauss-Legendre quadrature weight matrix **G** given by (B6) allows relations (A2) and (A7) to be satisfied numerically. In fact, as shown in Figure A1, the values of the Frobenius norm of the matrix difference $\mathbf{I} - \mathbf{F}'^T\mathbf{F}'$ divided by n_{coef} decrease very significantly, to the level of machine precision. The nonregular grid of Gauss-Legendre quadrature points with minimal size for achieving this goal has $n_{\text{point}} = (2\ell_{\max} + 1)(\ell_{\max} + 1)$, a result also known from, e.g., spherical harmonic transforms [e.g., *Reinecke and Seljebotn*, 2013], and we call it the optimal grid for a given truncation degree $\ell_{\max}$.

References

Abramowitz, M., and I. A. Stegun (1965), *Handbook of Mathematical Functions With Formulas, Graphs, and Mathematical Tables*, Dover, New York.

Balasis, G., and G. D. Egbert (2006), Empirical orthogonal function analysis of magnetic observatory data: Further evidence for non-axisymmetric magnetospheric sources for satellite induction studies, *Geophys. Res. Lett.*, 33, L11311, doi:10.1029/2006GL025721.

Brown, W. J., J. E. Mound, and P. W. Livermore (2013), Jerks abound: An analysis of geomagnetic observatory data from 1957 to 2008, *Phys. Earth Planet. Inter.*, 223, 62–76, doi:10.1016/j.pepi.2013.06.001.

Chulliat, A., and S. Maus (2014), Geomagnetic secular acceleration, jerks, and a localized standing wave at the core surface from 2000 to 2010, *J. Geophys. Res. Solid Earth*, 119, 1531–1543, doi:10.1002/2013JB010604.

Chulliat, A., E. Thébault, and G. Hulot (2010), Core field acceleration pulse as a common cause of the 2003 and 2007 geomagnetic jerks, *Geophys. Res. Lett.*, 37, L07301, doi:10.1029/2009GL042019.

Daniell, R. E., Jr., L. D. Brown, D. N. Anderson, M. W. Fox, P. H. Doherty, D. T. Decker, J. J. Sojka, and R. W. Schunk (1995), Parameterized ionospheric model: A global ionospheric parameterization based on first principles models, *Radio Sci.*, 30, 1499–1510, doi:10.1029/95RS01826.

Dumberry, M., and C. C. Finlay (2007), Eastward and westward drift of the Earth's magnetic field for the last three millennia, *Earth Planet. Sci. Lett.*, 254, 146–157.

Faynberg, E. B. (1975), Separation of the geomagnetic field into a normal and anomalous part, *Geomagn. Aeron.*, 15, 117–121.

Finlay, C. C., and A. Jackson (2003), Equatorially dominated magnetic field change at the surface of Earth's core, *Science*, 300, 2084–2086, doi:10.1126/science.1083324.

Finlay, C. C., A. Jackson, N. Gillet, and N. Olsen (2012), Core surface magnetic field evolution 2000–2010, *Geophys. J. Int.*, 189, 761–781, doi:10.1111/j.1365-246X.2012.05395.x.

Fujii, I., and A. Schultz (2002), The 3D electromagnetic response of the Earth to ring current and auroral oval excitation, *Geophys. J. Int.*, *151*, 689–709, doi:10.1046/j.1365-246X.2002.01775.x.

Gillet, N., V. Lesur, and N. Olsen (2010), Geomagnetic core field secular variation models, *Space Sc. Rev.*, *155*, 129–145, doi:10.1007/s11214-009-9586-6.

Gillet, N., D. Jault, C. C. Finlay, and N. Olsen (2013), Stochastic modeling of the Earth's magnetic field: Inversion for covariances over the observatory era, *Geochem. Geophys. Geosyst.*, *14*, 766–786, doi:10.1002/ggge.20041.

Golovkov, V. P., N. E. Papitashvili, Y. S. Tyupkin, and E. P. Kharin (1978), Separation of geomagnetic field variations on the quiet and disturbed components by the MNOC, *Geomagn. Aeron.*, *18*, 511–514.

Golovkov, V. P., T. I. Zvereda, and T. A. Chernova (2005), The IZMIRAN main magnetic field candidate model for IGRF-10, produced by a spherical harmonic-natural orthogonal component method, *Earth Planets Space*, *57*, 1165–1171.

Gubbins, D., and J. Bloxham (1987), Morphology of the geomagnetic field and implications for the geodynamo, *Nature*, *325*, 509–511, doi:10.1038/325509a0.

Le Huy, M., M. Alexandrescu, G. Hulot, and L. L. Jean-Mouël (1998), On the characteristics of successive geomagnetic jerks, *Earth Planets Space*, *50*, 723–732.

Le Huy, M., M. Mandea, L. L. Jean-Mouël, and A. Pais (2000), Time evolution of the fluid flow at the top of the core. Geomagnetic jerks, *Earth Planets Space*, *52*, 163–173.

Jackson, A., A. Jonkers, and M. Walker (2000), Four centuries of geomagnetic secular variation from historical records, *Philos. Trans. R. Soc. A*, *358*, 957–990.

Langel, R. A. (1987), The main field, in *Geomagnetism*, vol. 1, edited by J. A. Jacobs, pp. 249–512, Academic Press, London.

Lesur, V., I. Wardinski, M. Rother, and M. Mandea (2008), GRIMM: The GFZ Reference Internal Magnetic Model based on vector satellite and observatory data, *Geophys. J. Int.*, *173*, 382–394, doi:10.1111/j.1365-246X.2008.03724.x.

Mandea, M., and S. Macmillan (2000), International Geomagnetic Reference Field—The eighth generation, *Earth Planets Space*, *52*, 1119–1124, doi:10.1186/BF03352342.

Mandea, M., R. Holme, A. Pais, K. Pinheiro, A. Jackson, and G. Verbanac (2010), Geomagnetic jerks: Rapid core field variations and core dynamics, *Space Sci. Rev.*, *155*, 147–175, doi:10.1007/s11214-010-9663-x.

Olsen, N., M. Mandea, T. J. Sabaka, and L. Tøffner-Clausen (2009), CHAOS-2—A geomagnetic field model derived from one decade of continuous satellite data, *Geophys. J. Int.*, *179*, 1477–1487, doi:10.1111/j.1365-246X.2009.04386.x.

Olsen, N., H. Lühr, C. C. Finlay, T. J. Sabaka, I. Michaelis, J. Rauberg, and L. Tøffner-Clausen (2014), The CHAOS-4 geomagnetic field model, *Geophys. J. Int.*, *197*, 815–827, doi:10.1093/gji/ggu033.

Olson, P., and H. Amit (2006), Changes in Earth's dipole, *Naturwissenschaften*, *93*, 519–542, doi:10.1007/s00114-006-0138-6.

Pais, M. A., A. L. Morozova, and N. Schaeffer (2015), Variability modes in core flows inverted from geomagnetic field models, *Geophys. J. Int.*, *200*, 402–420, doi:10.1093/gji/ggu403.

Peixoto, J. P., and A. H. Oort (1992), *Physics of Climate*, Am. Inst. of Phys., New York.

Pinheiro, K. J., A. Jackson, and C. C. Finlay (2011), Measurements and uncertainties of the occurrence time of the 1969, 1978, 1991, and 1999 geomagnetic jerks, *Geochem. Geophys. Geosyst.*, *12*, Q10015, doi:10.1029/2011GC003706.

Preisendorfer, R. W. (1988), *Principal Component Analyses in Meteorology and Oceanography*, Elsevier, Amsterdam.

Pushkov, A. N., E. B. Faynberg, T. A. Chernova, and M. V. Fiskina (1976), Analysis of the spatial-temporal structure of the main geomagnetic field using the method of resolution into natural orthogonal components, *Geomagn. Aeron.*, *16*, 337–343.

Reinecke, M., and D. S. Seljebotn (2013), Libsharp—Spherical harmonic transforms revisited, *Astron. Astrophys.*, *554*, A112.

Rotanova, N. M., N. E. Papitashvili, and A. N. Pushkov (1982), The use of the method of natural orthogonal components to identify and analyze 60-year variations of the geomagnetic field, *Geomagn. Aeron.*, *22*, 1003–1009.

Sabaka, T. J., N. Olsen, and M. E. Purucker (2004), Extending comprehensive models of the Earth's magnetic field with Ørsted and CHAMP data, *Geophys. J. Int.*, *159*, 521–547, doi:10.1111/j.1365-246X.2004.02421.x.

Wardinski, I., and R. Holme (2006), A time-dependent model of the Earth's magnetic field and its secular variation for the period 1980–2000, *J. Geophys. Res.*, *111*, B12101, doi:10.1029/2006JB004401.

Wouters, B., and E. J. O. Schrama (2007), Improved accuracy of GRACE gravity solutions through empirical orthogonal function filtering of spherical harmonics, *Geophys. Res. Lett.*, *34*, L23711, doi:10.1029/2007GL032098.

Xu, W.-Y. (2002), Revision of the high-degree Gauss coefficients in the IGRF 1945–1955 models by using natural orthogonal component analysis, *Earth Planets Space*, *54*, 753–761.

Xu, W.-Y. (2003), Natural orthogonal component analysis of International Geomagnetic Reference Field models and its application to historical geomagnetic models, *Geophys. J. Int.*, *152*, 613–619, doi:10.1046/j.1365-246X.2003.01875.x.

Xu, W.-Y., and Y. Kamide (2004), Decomposition of daily geomagnetic variations by using method of natural orthogonal component, *J. Geophys. Res.*, *109*, A05218, doi:10.1029/2003JA010216.